PCCP

Accepted Manuscript

ROYAL SOCIETY OF CHEMISTRY

www.rsc.org/pccp

Journal Name

ARTICLE TYPE

Cite this: DOI: 10.1039/xxxxxxxxxx

Hybrid particle-field molecular dynamics simulation for polyelectrolyte systems

You-Liang Zhu,[a] Zhong-Yuan Lu,[b] Giuseppe Milano,[c] An-Chang Shi,[d] and Zhao-Yan Sun*[a]

Received Date
Accepted Date

DOI: 10.1039/xxxxxxxxxx

www.rsc.org/journalname

To achieve simulations on large spatial and temporal scales with high molecular chemical specificity, a hybrid particle-field method was proposed recently. This method is developed by combining molecular dynamics and self-consistent field theory (MD-SCF). The MD-SCF method has been validated by successfully predicting experimentally observable properties of several systems. Here we propose an efficient scheme for the inclusion of electrostatic interactions in the MD-SCF framework. In this scheme, charged molecules are interacting with the external fields that self-consistently determined from the charge densities. The method is validated by comparing structural properties of polyelectrolytes in solution obtained from the MD-SCF and particle-based simulations. Moreover, taking PMMA-b-PEO and $LiCF_3SO_3$ as an example, the enhancement of immiscibility between ion-dissolving block and inert block by doping lithium salts into the copolymer is examined by using the MD-SCF method. By employing GPU-acceleration, the high performance of the MD-SCF method with explicit treatment of electrostatics facilitates the simulation study of many problems involving polyelectrolytes.

1 INTRODUCTION

Although atomistic molecular dynamics (MD) simulation is an ideal tool to reveal microscopic mechanisms related to dynamics, thermodynamics, and structural properties of condensed matters and biological systems[1–3], describing the interactions of molecules in atomistic details is still a time-consuming task. Even with greatly enhanced computational power, present atomistic simulations are still extremely expensive on the mesoscopic time ($>\mu$s) and length (>100 nm) scales. Reducing the number of degrees of freedom by grouping a set of atoms together into one "super-atom" and keeping the key degrees of freedom related to a particular range of interest is a widely used coarse-graining[4–9]. The coarse-grained (CG) models are parameterized either in a "top-down" way by following a trial-and-error refinement process targeting the reproduction of key experimental structural or thermodynamic features (such as MARTINI model[10]), or in a "bottom-up" way by systematically reconstructing a CG Hamiltonian based on underlying more detailed simulations, such as iterative Boltzmann inversion[4,11] and inverse Monte Carlo methods[12]. However, these CG modelings normally target at a single resolution in which certain chemical details have to be neglected. Another strategy of coarse-graining that can simultaneously keep molecular details and improve computational efficiency is to treat systems within a single simulation on multiple levels of resolution, such as adaptive resolution and hybrid particle-field simulations. The former takes a small, well defined region of space at a higher level of detail, while the surrounding on a coarser, computationally more efficient level[13]. The latter, which includes a detailed model and field-derived interactions, is effective to study some collective properties involving slow ordering processes in which a large number of molecules participate, such as the phase transition in multi-component mixtures and the self-assembly of amphiphilic polymers.

In recent years, hybrid simulation techniques have been frequently proposed to save computational time by adopting self-consistent molecular field. For example, Sevink et al. introduced a hybrid model combining the elements of Brownian dynamics and dynamic density functional theory, for efficiently modeling vesicles with molecular detail[14]. Müller and coworkers proposed the particle and field representation of coarse-grained models in single chain in mean field (SCMF) method and applied it to

[a]State Key Laboratory of Polymer Physics and Chemistry, Changchun Institute of Applied Chemistry, Chinese Academy of Sciences, Changchun 130022, China. E-mail: zysun@ciac.ac.cn
[b]State Key Laboratory of Supramolecular Structure and Materials, Institute of Theoretical Chemistry, Jilin University, Changchun 130023, China
[c]Dipartimento di Chimica e Biologia, Università degli Studi di Salerno, via Ponte don Melillo, Fisciano, Salerno I-84085, Italy
[d]Department of Physics and Astronomy, McMaster University, Hamilton, Ontario L8S 4MI, Canada

† Electronic Supplementary Information (ESI) available: (a) The structure of electric double layers; (b) The phase behaviors of polyelectrolyte-surfactant complex. See DOI: 10.1039/b000000x/

homopolymer and block copolymer systems[15,16]. De Pablo and coworkers proposed a particle-based representation and density-based non-bonded interactions in Monte Carlo simulations and Jha et al. applied this method combined with electrostatic Green's function approach to study the phase transition behavior of non-interacting neutral and ionic nanogel in a solvent bath[17,18]. Hybrid models, due to their low computational cost and good performances in parallel applications, are becoming more and more popular[19–22]. More recently, the MD method combined with self-consistent field (SCF) theory was proposed by Milano et al., which is referred to as the "MD-SCF" approach[23,24]. Resorting to SCF to obtain the interactions applied in particle model, this hybrid particle-field (PF) method can efficiently accelerate the ordering processes of massive molecules by avoiding kinetic traps. The method has been validated by correctly reproducing phase behaviors of phospholipids in aqueous solutions[25,26] and the dependence of morphologies on concentration and temperature of pluronic-water mixtures[27]; it also has applications on predicting the interaction of micellar drug nanocarriers and biomembranes[28], and relaxing all-atom structures of polymer melts[29]. However, the lack of explicit treatment of long-range electrostatic interactions in the original framework makes it unable to study systems containing charged molecules.

Charged biomolecules and polyelectrolytes play an important role in life science and material science[8,30,31]. However, these charged macromolecules are extremely difficult to be studied by ordinary MD simulations. The difficulties originate from two aspects: First, chain entanglements largely hamper the relaxation of polymer chains. To understand the level of computational effort required for polymer simulations: the longest relaxation process of an entangled polymer melt of length N scales at least as N^3. Fortunately, computational costs of the PF method are mainly related to system size rather than to the chain length[29]. Second, the calculation of Coulombic interactions in MD is very time consuming due to their long-range nature. The Coulombic interaction between two point charges decays slowly as their distance increases. The spherical cutoff treatment used for short-ranged interactions (such as Lennard-Jones) is inadequate for Coulombic interactions because arbitrary truncation can lead to artifacts. In addition, for MD with periodic boundary conditions, the Coulombic interactions from image charges have to be considered. As such, long-range Coulombic interactions in MD have to be handled in some special ways[32–35]. A classic method that properly handles the Coulombic interactions in periodic systems is the Ewald summation method[32]. In the Ewald summation, the Coulombic interaction is split into two parts, i.e., a short-range part that can be calculated accurately using cutoff treatment and a long-range part that can be calculated in reciprocal-space using a Fourier series. However, the standard Ewald summation at best scales as $O(N^{3/2})$ and therefore becomes inefficient for large systems. Some variants of the Ewald summation, such as the particle-particle particle-mesh method (PPPM)[36], particle-mesh Ewald method (PME)[37,38], and Non-Uniform FFTs method (ENUF)[39,40], have been developed to accelerate calculation by taking advantage of fast Fourier transform (FFT), leading to an $O(N\log N)$ scaling of computation time.

With the aforementioned discussion in mind, it is obvious that computational efficiency is the key bottleneck for MD simulations of the collective behavior of charged macromolecules. In this study, we propose an efficient electrostatic treatment in the framework of MD-SCF. Specifically, we consider a PF electrostatic interaction scheme taking advantage of the PF interaction nature of MD-SCF. The accuracy of the electrostatic interactions is tunable according to the resolution of the field description. The charged macromolecules are interacting with the external field that implicitly depends on the distribution of charge densities and is hereafter referred to as "E-field". The field quantities including electrostatic potentials and their derivatives are defined on a three-dimensional lattice with periodic boundary conditions. According to the Ewald summation, electrostatic potential is split into two parts. By matching the short-range energy to Flory-Huggins interaction parameter, the short-range part of electrostatic interactions on lattice points is evaluated by collecting the contributions from the surrounding charges. The long-range part on lattice points can be calculated by solving the Poisson's equation after defining the charge densities on lattice. The derivatives of energies which are used for the calculation of forces are interpolated from the energy distributions.

In previous work, we have developed the GPU-accelerated computation algorithm of MD-SCF method incorporated in GALAMOST (downloadable at *http://galamost.com*). GALAMOST is a versatile MD package optimized for fully utilizing computational power of GPU[41]. To accelerate the simulation of charged macromolecular systems, the electrostatic calculation based on MD-SCF has also been implemented in GALAMOST. Combining the new framework of the calculation of electrostatic interactions based on MD-SCF and the high efficiency of GPU computation, we can tackle problems with larger temporal and spatial scales in simulations of charged macromolecules.

2 MODEL AND METHOD

2.1 The MD-SCF approach

The scales at which the phase behavior and self-assembly properties of macromolecules are studied by SCF approach can not be reached easily by ordinary MD simulations[42,43]. However, macromolecules in SCF are ideally modeled by using the standard model, i.e., with assumptions such that (1) incompressibility of the system, (2) continuous Gaussian chains, and (3) the δ-function type interaction. Moreover, SCF theory is normally treated as a mean-field theory neglecting the fluctuations. On the other hand, molecular dynamics simulations include the molecular details of the system. Therefore, to combine advantages of SCF and MD, the MD-SCF method that applies the soft potentials derived from SCF theory in particle models of MD has been proposed[23]. In this hybrid PF method, a molecule is regarded to be interacting with surrounding molecules not directly but through density fields. The density fields are constructed from the spatially inhomogeneous density distributions of segments of independent molecules. The interaction formulism in MD-SCF is derived from the minimization of the free energy by applying SCF theory. However, all intramolecular interaction terms (bond, an-

gle, etc.) in MD-SCF are usually considered as the conventional forms in MD. The different scales of interactions can be mitigated by treating the intramolecular interactions by propagating the system configuration via a small time step, but treating soft intermolecular interactions derived from density fields by updating the density fields via many of these small time steps[25].

According to the spirit of SCF theory, the main issue is to derive the partition function of a single molecule in an external mean field and further to obtain a suitable expression of the potential $V(\mathbf{r})$ and its derivative. Starting from the partition function, the expression of $V(\mathbf{r})$ can be obtained by using saddle point approximation. Details of the derivation of $V(\mathbf{r})$ are given in previous publications[23–26]. For a simple system with short-range pairwise interactions, the density-dependent external potential can be directly obtained:

$$V_K(\mathbf{r}) = k_BT\sum_{K'}\chi_{KK'}\phi_{K'}(\mathbf{r}) + \frac{1}{\kappa}(\sum_K \phi_K(\mathbf{r}) - 1), \tag{1}$$

where each component is specified by an index K, κ is the compressibility, χ represents the mean field parameter which is related to the Flory−Huggins parameter, and ϕ is the density distribution. In the case of a mixture of two components A and B, the mean field potential acting on a particle of type A at position $\mathbf{r}$ is given by

$$V_A(\mathbf{r}) = k_BT[\chi_{AA}\phi_A(\mathbf{r}) + \chi_{AB}\phi_B(\mathbf{r})] + \frac{1}{\kappa}(\phi_A(\mathbf{r}) + \phi_B(\mathbf{r}) - 1). \tag{2}$$

Then the force acting on particle A at position $\mathbf{r}$ imposed by the interaction with the density field is

$$\begin{aligned} F_A(\mathbf{r}) &= -\frac{\partial V_A(\mathbf{r})}{\partial \mathbf{r}} \\ &= -k_BT(\chi_{AA}\frac{\partial\phi_A(\mathbf{r})}{\partial\mathbf{r}} + \chi_{AB}\frac{\partial\phi_B(\mathbf{r})}{\partial\mathbf{r}}) - \frac{1}{\kappa}(\frac{\partial\phi_A(\mathbf{r})}{\partial\mathbf{r}} + \frac{\partial\phi_B(\mathbf{r})}{\partial\mathbf{r}}). \end{aligned} \tag{3}$$

2.2 The treatment of electrostatic interactions in MD-SCF

In the framework of MD-SCF, electrostatic interactions between charged molecules are not considered directly, but through the E-fields, which in turn depend on the spatially inhomogeneous distributions of charge densities. In order to represent the E-fields, the simulation box ($\mathbf{L}_1$, $\mathbf{L}_2$, $\mathbf{L}_3$) is divided into $N_1 \times N_2 \times N_3$ cells (where N_α is the number of cells in the $\mathbf{L}_\alpha$ direction, with $\alpha = 1,2,3$). The location of the lattice points can be given by $\mathbf{l} = (l_1\mathbf{L}_1/N_1,\ l_2\mathbf{L}_2/N_2,\ l_3\mathbf{L}_3/N_3)$ (l_α is integer and $0 \le l_\alpha < N_\alpha$). The total Coulomb energy is expressed as

$$E = \frac{1}{2}\sum_i q_i\psi(\mathbf{r}_i), \tag{4}$$

where $\psi(\mathbf{r})$ is the electrostatic potential, and q is the reduced charge. $\psi(\mathbf{r})$ can be obtained by collecting the contributions of all particles

$$\psi(\mathbf{r}) = k_BTl_B\sum_{\mathbf{n}}\sum_j \frac{q_j}{|\mathbf{r}-\mathbf{r}_j+\mathbf{n}|}, \tag{5}$$

where the outer sum is over the vectors $\mathbf{n} = n_1\mathbf{L}_1 + n_2\mathbf{L}_2 + n_3\mathbf{L}_3$ with periodic boundary conditions, $l_B = e^2/4\pi\varepsilon_0\varepsilon_r k_BT$ is the Bjerrum length; e, ε_0, and ε_r are elementary charge, electric permeability of vacuum, and relative dielectric constant, respectively. Using the Ewald summation, the electrostatic potential can be split into two parts $\psi(\mathbf{r}) = \psi^L(\mathbf{r}) + \psi^S(\mathbf{r})$ with

$$\psi^S(\mathbf{r}) = k_BTl_B\sum_{\mathbf{n}}\sum_j \frac{q_j\mathrm{erfc}(\alpha|\mathbf{r}-\mathbf{r}_j+\mathbf{n}|)}{|\mathbf{r}-\mathbf{r}_j+\mathbf{n}|}, \tag{6}$$

$$\psi^L(\mathbf{r}) = \sum_{\mathbf{m}\neq 0}\hat{\psi}^L(\mathbf{m})\exp(i\mathbf{m}\cdot\mathbf{r}), \tag{7}$$

where $\hat{\psi}^L$ in Eq. 7 is the long-range part of the electrostatic potential in reciprocal space. With the Gaussian distribution of charge density, the Poisson's equation can be solved in reciprocal space, resulting in the expression of $\hat{\psi}^L$ as

$$\begin{aligned} &\hat{\psi}^L(\mathbf{m}) = C(\mathbf{m})\sum_{j=1}^N q_j\exp(-i\mathbf{m}\cdot\mathbf{r}_j) \\ &\text{with } C(\mathbf{m}) = 4\pi k_BTl_B\frac{\exp(-\mathbf{m}^2/4\alpha^2)}{V\mathbf{m}^2}, \end{aligned} \tag{8}$$

where $\mathbf{m} = 2\pi(m_1\mathbf{L}_1^* + m_2\mathbf{L}_2^* + m_3\mathbf{L}_3^*)$ with m_1, m_2, m_3 integers not all zero, V is the volume of simulation box. The conjugate reciprocal vectors $\mathbf{L}_\alpha^*$ are defined by the relations $\mathbf{L}_\alpha^*\cdot\mathbf{L}_\beta = \delta_{\alpha\beta}$ (the Kronecker delta), for $\alpha,\beta = 1,2,3$.

By linearly interpolating the complex exponentials $\sum_{j=1}^N q_j\exp(-i\mathbf{m}\cdot\mathbf{r}_j)$ in Eq. 8 (see interpolation details in APPENDIX A or Ref.[38]), we obtain the approximate complex exponentials at lattice points. Further, we can rewrite $\hat{\psi}^L(\mathbf{m})$ as

$$\hat{\psi}^L(\mathbf{m}) = C(\mathbf{m})F(Q)(m_1,m_2,m_3), \tag{9}$$

where Q (see definition in APPENDIX A) can be regarded as the charge densities at lattice points and $F(Q)$ is the discrete Fourier transform (DFT). The long-range part of the electrostatic potential at the lattice point of spacial position $\mathbf{l}$ can be rewritten in total DFT form

$$\begin{aligned} \psi^L(\mathbf{l}) &= \sum_{\mathbf{m}\neq 0}\hat{\psi}^L(\mathbf{m})\exp(i\mathbf{m}\cdot\mathbf{l}) \\ &= \sum_{m_1=0}^{N_1-1}\sum_{m_2=0}^{N_2-1}\sum_{m_3=0}^{N_3-1}\hat{\psi}^L(\mathbf{m})\exp\left[2\pi i\left(\frac{m_1l_1}{N_1} + \frac{m_2l_2}{N_2} + \frac{m_3l_3}{N_3}\right)\right] \\ &= F^{-1}[CF(Q)](l_1,l_2,l_3). \end{aligned} \tag{10}$$

Thereby, the long-range part of the electrostatic potential can be obtained with a forward and a backward DFT. The DFT can be efficiently calculated by employing FFT library, such as cuFFT on GPUs.

The short-range part of electrostatic interactions given by Eq. 6 is usually considered as pairwise interaction in MD. However, for PF simulations, only mean field parameters are applicable. To this end, a χ_e parameter for short-range part of electrostatic interactions can be obtained by following the Flory-Huggins approach

for lattice models

$$\chi_e = \frac{z_{CN}}{k_B T}\left[\frac{2u_{CC'} - (u_{CN} + u_{C'N})}{2}\right] = z_{CN} l_B \frac{\mathrm{erfc}(\alpha\sigma)}{\sigma}, \qquad (11)$$

where the parameter z_{CN} is the coordination number which takes a value of 6 for a three-dimensional cubic lattice; $u_{CC'}$, u_{CN}, and $u_{C'N}$ are the pairwise short-range electrostatic energies between a pair of adjacent lattice sites, with $u_{CC'} = k_B T l_B \mathrm{erfc}(\alpha\sigma)/\sigma$ for the lattice sites occupied by charged particles and being related to the diameter σ of the coarse-grained particles, $u_{CN} = u_{C'N} = 0$ for the lattice sites occupied by one particle with elementary charge and the other one being neutral. Thereby, the short-range part of the electrostatic potential at lattice point of spacial position $\mathbf{l}$ can be obtained in the density field manner[23]

$$\psi^S(\mathbf{l}) = \chi_e Q(l_1, l_2, l_3) k_B T. \qquad (12)$$

The approximation of short-range electrostatic potential from linear interpolation also gives a similar expression of Eq. 12, as shown in APPENDIX B. The electric fields $\psi'(\mathbf{l})$, which are used for the calculation of electrostatic forces, can be obtained by linear interpolation between lattices with

$$\psi_1'(l_1,l_2,l_3) = \frac{1}{2}[\psi(l_1+1,l_2,l_3) - \psi(l_1-1,l_2,l_3)]N/|\mathbf{L}_1|,$$

$$\psi_2'(l_1,l_2,l_3) = \frac{1}{2}[\psi(l_1,l_2+1,l_3) - \psi(l_1,l_2-1,l_3)]N/|\mathbf{L}_2|,$$

$$\psi_3'(l_1,l_2,l_3) = \frac{1}{2}[\psi(l_1,l_2,l_3+1) - \psi(l_1,l_2,l_3-1)]N/|\mathbf{L}_3|. \qquad (13)$$

With the established E-fields, the electrostatic energy and force of charged particles at arbitrary positions can be calculated reversely by linear interpolation. The linear interpolation scheme is used in E-fields to keep consistent with the one in density fields. It should be mentioned that the self-energy $k_B T l_B q_j^2 \alpha/\sqrt{\pi}$ should be removed from the total electrostatic energy of particle j.

3 RESULTS AND DISCUSSION

3.1 Polyelectrolyte solution

To validate our treatment of the electrostatic interactions, we have performed MD-SCF simulations of a linear polyelectrolyte chain in solution and compared its structural properties at different dielectric constants with those from reference particle-based (PP) simulations. The polyelectrolyte molecule contains 100 repeating CG particles with 20% of these particles carrying a negative charge. The charged particles are equally spaced along the polymer backbone. In addition, the system contains 20 monovalent CG cations as counterions and 7430 solvent particles. The particles are classified as P (polyelectrolyte), C (counterion), and S (solvent) types, respectively. Initially, the polyelectrolyte chain with equilibrium bond length of 0.4 nm is placed with a random configuration in a cubic box with a volume of $(10\ \mathrm{nm})^3$. A spring constant of 1000 kJ/mol is used for the harmonic bond interactions. The mass of all CG particles is set as 72 amu. The simulations are performed at 300 K.

In reference PP simulations, all Lennard-Jones (LJ) interactions $V_{LJ}(r) = 4\varepsilon[(\sigma/r)^{12} - (\sigma/r)^6]$ are characterized with $\varepsilon = 1.0$ kJ/mol and $\sigma = 0.47$ nm. For PF simulations, the parameter $\chi_{KK'}$ in Eq. 1 that represents the mean field parameter for the interaction of a particle of type K with the density fields due to particles of type K' is needed. A simple choice of the parameter can be obtained by following Flory-Huggins approach for the calculation of χ parameters for lattice models

$$\chi_{KK'} = \frac{z_{CN}}{k_B T}\left[\frac{2u_{KK'} - (u_{KK} + u_{K'K'})}{2}\right], \qquad (14)$$

where $u_{KK'}$ is the pairwise interaction energy between a pair of adjacent lattice sites occupied by the units of types K and K'. It can be set as $u_{KK'} = -\varepsilon_{KK'}$, where $\varepsilon_{KK'}$ is the LJ parameter. According to Eq. 15, the derived mean field parameters for the PF simulations are $\chi_{KK'} = 0$ (for K, $K' = P$, C, S), which correspond to an athermal condition. The excluded volume effects between particles are taken into account in the field description by imposing the incompressibility condition. The criterion to determine the value of the compressibility κ in Eq. 1 is reproducing the value of average density fluctuations. In particular, using values of $\kappa \approx 8RT$ (where R is the gas constant and T temperature), average density fluctuations were found in agreement with the reference PP simulation[25]. Thereby, the only tunable parameters are grid size and the parameter α in Eq. 6. The α, which is related to the Gaussian distribution width of the charge, controls the relative rate of convergence of the direct and the reciprocal sums. However, the total electrostatic potential energy is invariant to α. We consider the Ewald coefficient α as 4.2 nm^{-1}, following Ref.[38]. The same grid size l and update frequency $\triangle t_{\mathrm{update}}$ of density field are applied in E-field. For this system, the update frequency is chosen as $\triangle t_{\mathrm{update}} = 1$ for maximum precision. Here, we test three distinct grid sizes: $l = 0.625$ nm ($\sim 1.33\ \sigma$), $l = 0.313$ nm ($\sim 0.67\ \sigma$), and $l = 0.238$ nm ($\sim 0.51\ \sigma$), which correspond to 16^3, 32^3, and 42^3 lattice points, respectively.

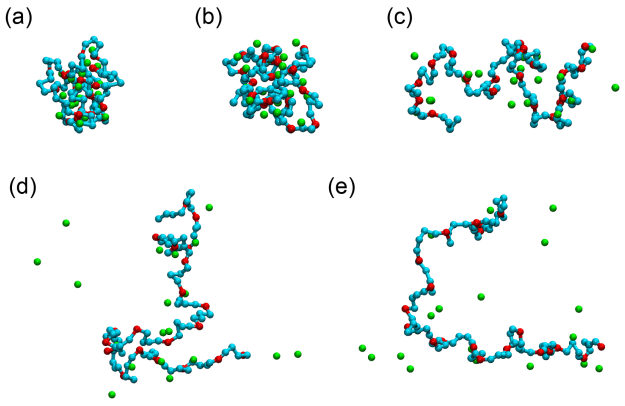

Fig. 1 Typical conformations of a polyelectrolyte chain in solution at relative dielectric constant of (a) 3.9, (b) 7.8, (c) 15.6, (d) 20.0, and (e) 78.0, respectively. These snapshots are taken from the PF simulations with the grid size of l = 0.238 nm.

By increasing dielectric constant, we can observe the globule-coil-stretch transition of the polyelectrolyte chain. Typical equilibrium chain conformations at different dielectric constants in

PF simulations are shown in Fig. 1. At low dielectric constants, the polyelectrolyte chain is in a globule state due to the strong electrostatic attractions between negative charges of the polyelectrolyte chain and positive charges of the counterions. While at high dielectric constants, the weak electrostatic attractions between opposite charges can not constrain the counterions to the polyelectrolyte chain. In this case, the electrostatic repulsions between the bound negative charges on the polyelectrolyte backbone result in an extended chain conformation. At moderate dielectric constants, the two effects compete and the polyelectrolyte is a coil. At the relative dielectric constant (ε_r) of about 16, the radius of gyration (R_g) of the polyelectrolyte chain is close to the corresponding neutral chain (about 2.71 nm, the PF and PP simulations give the same value).

The dependence of R_g on relative dielectric constant is given in Fig. 2. The curves of R_g vs. ε_r for different field resolutions are compared with the one obtained by reference PP simulations (performed by using GROMACS with PME method[44]). Although the grid size affects the R_g values (especially at low dielectric constants), the globule-coil-stretch transition in PF simulations agrees well with that in reference PP simulations. Similar transition had also been reported in previous works[35,45]. When the grid size is smaller (e.g. l = 0.313 nm and l = 0.238 nm) than the diameter of particles (σ = 0.47 nm), the R_g values at a series of dielectric constants obtained by our PF simulations are very close to those obtained by reference PP simulations.

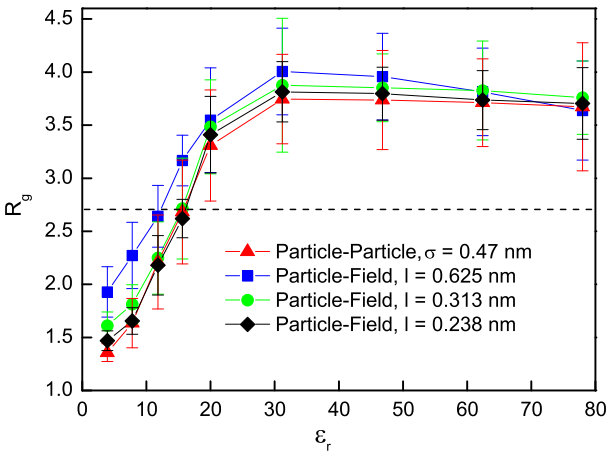

Fig. 2 The radius of gyration R_g of a polyelectrolyte chain in solution with different relative dielectric constants from PF simulations and PP simulations. The horizontal dash line indicates the equilibrium R_g of the neutral polymer without charges.

We analyzed the pair correlations between polyelectrolyte particles (including charged and neutral ones) and counterions. As shown in Fig. 3, the radial distribution function shows typical behavior of the polyelectrolyte chain in dilute solution, i.e., the curves have a correlation hole at short distances and a peak followed by further decaying at longer distance and finally reach zero; the height of the peak of the correlation between charged particles and counterions is much higher than the one between neutral particles and counterions due to the electrostatic attractive interactions. When the spatial resolution of the density field becomes smaller than σ, the data of PF simulations show a deep correlation hole at short distances and similar decaying behavior as in PP simulations. The main differences in the behavior of the radial distribution functions between the PP and hybrid PF simulations can be ascribed to the mean field approximation in PF treatment, which results in weak correlation at short distances.

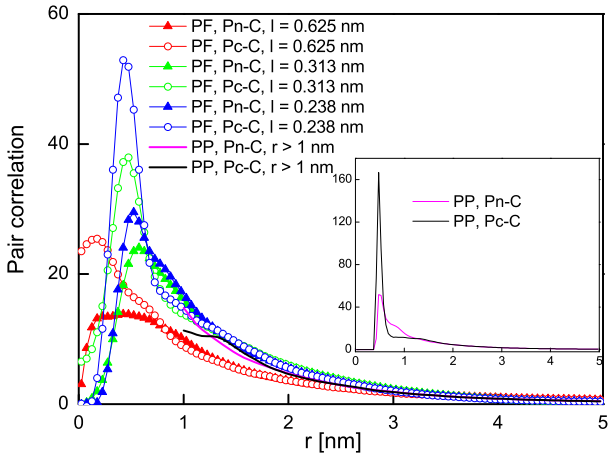

Fig. 3 The pair correlations between polyelectrolyte particles and counterions at relative dielectric constant of 11.7. The charged and neutral polyelectrolyte particles are indicated by Pc and Pn, respectively.

3.2 Microphase separation of block copolymers containing charged blocks

Poly(ethylene oxide) (PEO)-based copolymers doped with salt ions, such as lithium ion (Li^+), are potential candidates for electrolytes used in solid-state rechargeable lithium batteries. Since the binding energy between Li^+ and oxygen is very large, PEO with its bound Li^+ ions is effectively a polyelectrolyte. A promising candidate of polymer electrolyte with both high ionic conductivity and dimensional stability consists in covalently bonding an ion-dissolving block, such as PEO, to an nonconducting block, such as poly (methyl methacrylate) (PMMA), thereby forming a block copolymer. Block copolymers are usually ordered at low temperature due to the immiscibility between the block segments. These materials will undergo an order/disorder transition (ODT), accompanied by a solid-like/liquid-like rheological transition, when heated to a sufficiently high temperature. However, for PMMA-b-PEO copolymer, the high miscibility between PEO and PMMA makes this copolymer essentially segmentally mixed at all temperatures. The disordered liquid state without the addition of a common solvent is clearly desirable for melting processing. The degree of immiscibility between PEO and PMMA can be dramatically increased by even small additions of lithium salts, such as $LiCF_3SO_3$, which results in microphase separation and the formation of ordered structures[46].

Here we use MD-SCF method to study the structure formation of PMMA-b-PEO block copolymers by adding salts. According to the formulation of MD-SCF method, the intramolecular terms (including bond, angle, and dihedral interactions) have the conventional forms as in MD simulations. Their functional forms and

parameters can be chosen as those in the original MARTINI force field. We have modeled the PMMA-b-PEO copolymer by mapping the PMMA monomer to two CG beads: One bead (A type) for backbone and the other bead (B type) for side chain, and mapping the PEO monomer to one bead (C type). The schematic CG strategy is shown in Fig. 4. The intramolecular interactions of PEO CG beads have been given in MARTINI force field, which were derived in a bottom-up manner from the all-atom simulations[47]. For the intramolecular interactions of PMMA CG beads that are not yet included in MARTINI force field, we have employed the analytical potentials that were also derived from bottom-up coarse-graining by mapping the structural properties of PMMA to results of all-atom simulations[48]. With the CG model, we consider PMMA-b-PEO copolymer with two chain lengths, $(AB)_{10}C_{20}$ and $(AB)_{50}C_{100}$, respectively. These two copolymers have the same PEO volume fraction (f_{PEO}) with $f_{PEO} \approx 0.5$. The doping of Li cations is treated in our model by randomly choosing some C beads as charged beads, each carrying a positive elementary charge. The same number of "free" beads (D type), each carrying a negative elementary charge, are added as counterions. According to previous studies, the grid size l and update frequency $\triangle t_{update}$ can be tuned to obtain maximum computational performance without an obvious loss of precision[25,26]. Therefore, a grid size $l = 1.5\sigma$ (0.625 nm) and an update frequency $\triangle t_{update} = 10$ are employed in the simulations. The update frequency can be extended to a larger value. However, we find that the computational performance increases little with $\triangle t_{update}$ when $\triangle t_{update} \geq 10$ (see Table 1).

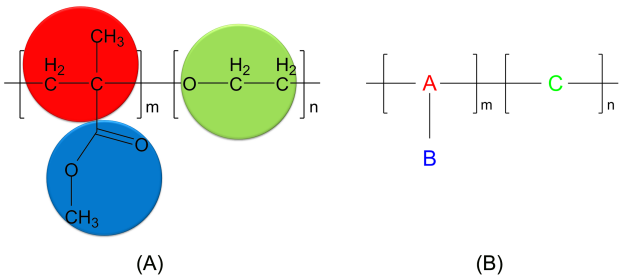

Fig. 4 The coarse-graining scheme of PMMA-b-PEO.

For the $(AB)_{10}C_{20}$ system, 1200 chains are initially randomly placed in a cubic box with a volume of $(15\ nm)^3$. The mean field parameter $\chi = \chi_{AC} = \chi_{BC}$ can be estimated from solubility parameters (δ) by[49]

$$\chi_{KK'} = \frac{V_b(\delta_K - \delta_{K'})^2}{RT}, \qquad (15)$$

where V_b is the volume of CG units. δ_{PMMA} for 10-monomer block and δ_{PEO} for 20-monomer block were given by atomistic MD simulations[50] with $\delta_{PEO} = 4.04\ (cal/cm^3)^{0.5}$ and $\delta_{PMMA} = 6.83\ (cal/cm^3)^{0.5}$. Here, $V_b \approx 62.5\ cm^3/mol$, thereby the χ parameter is about 0.82 at the temperature of 300 K. For both neat and salt-doped systems, 1.2 μs MD-SCF simulation is enough to obtain equilibrium structures. In our hybrid PF simulations, the neat system is disordered at 300 K with $\chi = 0.82$, which is in consistent with the fact that PMMA-b-PEO copolymers are segmentally mixed at all temperatures[46]. In our simulations, the neat system is disordered mainly due to strong fluctuations at short chain lengths.

Recently, Nakamura and Wang demonstrated the important role of dielectric self energy in phase separation of block copolymers when there is a difference in the relative dielectric constant between the two blocks[51]. Sing et al. scrutinized dielectric inhomogeneity effect and electrostatic cohesion effect, and demonstrated their different behaviors[52]. The dielectric inhomogeneity essentially changes the phase behavior by shifting the phase diagram vertically. While the electrostatic cohesion among charged monomers and ions tilts the phase diagram. To understand the electrostatic cohesion effect, we refer to the case of a polyelectrolyte in solution described in the last subsection. At low relative dielectric constants, strong electrostatic interactions energetically favour a state of high densities of charges, which overcome the entropy of counterions. In our study, we consider $\varepsilon_{r,AB} = \varepsilon_{r,C} = 7.3$ to highlight the effect of electrostatic cohesion[53]. It should be noted that the electrostatic interactions are only included in the salt-doped system. With the diameter of charged particles $\sigma = 0.47$ nm and the Ewald coefficient $\alpha = 4.2\ nm^{-1}$, the parameter l_B and χ_e (see Eq. 11) can be derived, specifically as $l_B = 7.67$ nm and $\chi_e = 0.51$ for this system.

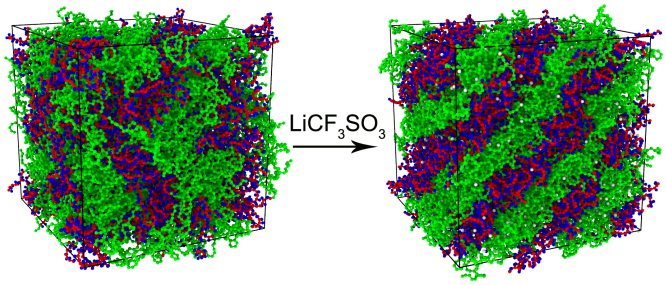

Fig. 5 The snapshots of neat and salt-doped $(AB)_{10}C_{20}$ systems, both at $\chi_{AC} = \chi_{BC} = 0.82$. The A, B, C, and D types are shown in red, blue, green, and white, respectively.

At a temperature of 300 K, the salt-doped system becomes phase separated into a lamellar structure at a χ_{ODT} of 0.76 for $[Li^+]$:[EO] = 1:20, 0.72 for $[Li^+]$:[EO] = 2:20, and 0.80 for $[Li^+]$:[EO] = 3:20. The mean field theory predicted that the electrostatic cohesion enhances phase separation in primarily low charged-block fraction materials, and either enhances or depresses phase separation in high charged-block fraction materials depending on salt-doping ratio[52]. In our simulations, the electrostatic cohesion effect enhances phase separation not linearly with the increase of salt-doping ratio, which qualitatively agrees with the mean field prediction. It can be attributed to that the entropic penalty, which suppresses phase separation, increases as the number of charged particles increases. The snapshots of both neat and salt-doped systems at $\chi = 0.82$ and $[Li^+]$:[EO] = 1:20 are shown in Fig. 5. The density profiles of one block (PMMA) and counterions along the normal direction of layers are analyzed for the salt-doped system at $\chi = 0.80$ and 0.88 and $[Li^+]$:[EO] = 1:20, as

shown in Fig. 6. According to the density profiles, the thickness of periodic layers of salt-doped systems does not change much ($d \approx 5.1$ nm). In experiments, the thickness of periodic layers increases with the salt-doping ratio for PEO-b-PS copolymer[54]. However, the changes of the thickness are not obvious at different salt-doping ratios for PMMA-b-PEO and PCL-b-PEO[46,55].

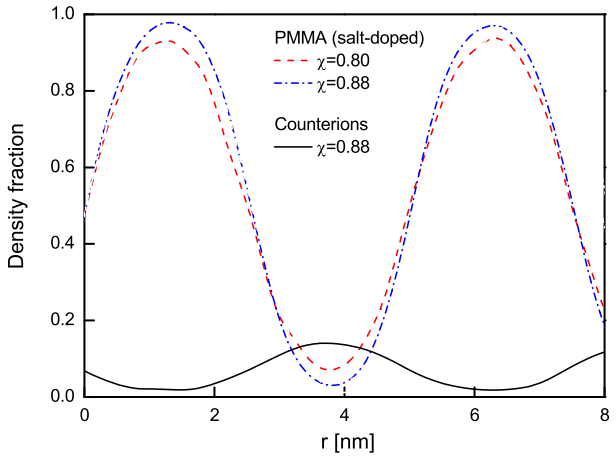

Fig. 6 The density fraction profiles of PMMA block and counterions of $(AB)_{10}C_{20}$ systems along the normal of layers. The value of density fraction of counterions has been magnified five times to guide eyes.

For the $(AB)_{10}C_{20}$ system, we measure the performances of the PF method and compare them with those of the reference PP simulations all implemented on GPU. The performances of the PF simulations on different grid sizes which correspond to different number of lattice points and different update frequencies are shown in Table 1. The PF simulations gain a speed-up ratio from 11.6 to 15.3 as compared to the reference PP simulations. The computational efficiency of the PF approach allows the speed up of the simulations by a factor of up to 10 for the considered systems. To have an idea about the efficiency of PF method for the systems considered in this paper, we take 1,920 $(AB)_{50}C_{100}$ as an example. It contains a total of 393,600 beads, and the performance is about 0.39 μs/day on 1 GTX 980 GPU. The snapshot of the system in equilibrium is shown in Fig. 7. As we can see, the well separated lamellar phase can be formed for these long chain systems by using PF method.

Table 1 The comparison of performance between the PF simulations achieved by GALAMOST and the PP simulations achieved by GROMACS[44] all on a single GPU (GTX 980). The system contains total 49,200 particles; 2,400 particles of them are charged. All simulations are performed in single precision operations. The update frequency is in the unit of time steps.

Model	Grid size	$\triangle t_{update}$	Highest Δt	Performance	Speed-up
PP			10 fs	144.8 ns/day	1.0
PF	0.469 nm	1	30 fs	1674.4 ns/day	11.6
PF	0.625 nm	1	30 fs	1783.3 ns/day	12.3
PF	0.625 nm	5	30 fs	2115.1 ns/day	14.6
PF	0.625 nm	10	30 fs	2203.2 ns/day	15.2
PF	0.625 nm	20	30 fs	2210.5 ns/day	15.3

3.3 Application scope and limitations

The PF method is scalable at simulated spatial and temporal scales. It can reproduce the essential structural features of electric double layers given by MD [see section (a) in the ESI†]. In addition, it also can present the phase behaviors of a polyelectrolyte-surfactant complex system predicted by dissipative particle dynamics [see section (b) in the ESI†]. The difference of density profiles of ions in electric double layers between PP and PF simulations can be ascribed to the softness nature of interactions in PF simulation. These tests further validate the method. However, the strength of this method rather becomes visible when focusing on phase transitions or ordering effects of long charged macromolecules, meanwhile with higher molecular chemical specificity in model.

Unlike MD simulations, in which accurate interactions are pursued, PF simulations implement the mean field interactions derived from both density field and E-field. Therefore, the strong electrostatic attractions and core repulsions at much shorter distances in MD simulations which come to compact ion clusters or tight ion pairs can not be presented in PF formulism. In addition, the calculation of direct excluded-volume interactions is avoided inherently by the method. With this aspect, the dynamics associated to the chain entanglements can not be truly reflected due to that chain molecules are allowed to cross each other. However, the lack of entanglement limitations accelerate chains movement, which facilitates a rapid convergency of simulated phase behaviors or self-assembled structures.

4 CONCLUSIONS

In this work, we propose a PF scheme for the calculation of electrostatic interactions in the framework of MD-SCF. Based on

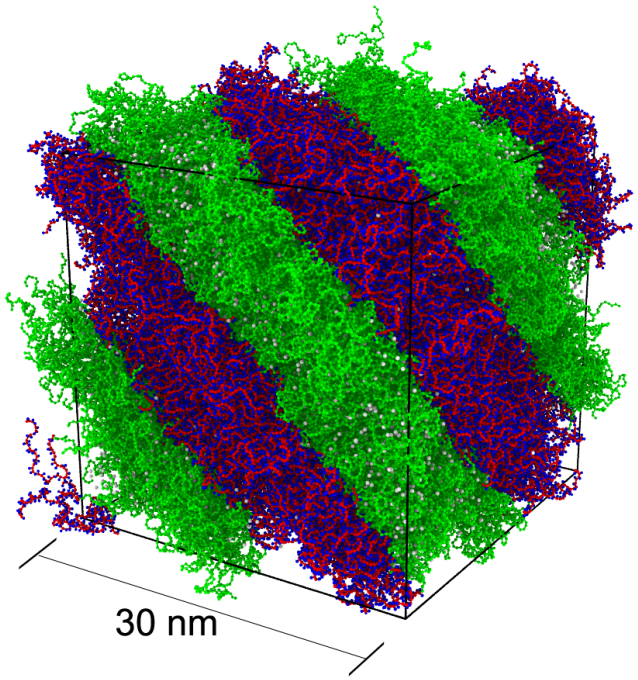

Fig. 7 The snapshot of phase separated structure of $(AB)_{50}C_{100}$ system.

the Ewald summation, electrostatic potential is split into a short-range part and a long-range part. The short-range part is evaluated by matching the short-range electrostatic potential to Flory-Huggins χ-parameter and collecting the contributions from the particles around grid points. The long-range part is treated by discrete Fourier transform of the charge densities at lattice points and the computation can be accelerated by the FFT with cuFFT library on GPUs. The resolution of describing electrostatic interactions can be tuned by changing the grid size of E-fields. This electrostatic method is validated by comparing the configurations of a polyelectrolyte chain at different dielectric constants in salt-free, athermal solution to those of reference PP simulations. Furthermore, we have employed MD-SCF with electrostatics to study the salt-induced phase separation of PMMA-b-PEO block copolymers. By employing GPU-acceleration, the performances of this PF method are evaluated at different grid sizes and update frequencies and compared with those of PP method by using GROMACS running on CPUs. The MD-SCF with electrostatics shows high computational performance and has a great potential in the studies of a vast kind of problems involving polyelectrolytes and biomolecules. We believe that, including the new theoretical developments, our PF scheme has a broad and timely interest in the soft matter community.

ACKNOWLEDGMENT

This work is subsidized by the National Basic Research Program of China (973 Program, 2012CB821500) and supported by National Science Foundation of China (21222407, 21404102, 21474111). ZYL also thanks the support from Jilin Province Science and Technology Development Plan (20140519004JH). YLZ gratefully acknowledges the support of China Postdoctoral Science Foundation (2014M551200) and the support of NVIDIA Corporation with the donation of the Tesla K40 GPU used for this research. ACS acknowledges the support by the Natural Science and Engineering Research Council of Canada.

APPENDIX A

In order to employ the fast Fourier transform, we need to approximate the complex exponentials appearing in the expression of $\hat{\psi}^L(\mathbf{m})$ from particles to lattice points. We denote the scaled fractional coordinates by $u_{\alpha j} = N_\alpha \mathbf{L}_\alpha^* \cdot \mathbf{r}_j$ ($0 \le u_{\alpha j} < N_\alpha$, for $\alpha = 1,2,3$). Then we can rewrite the complex exponentials as

$$\sum_{j=1}^{N} q_j \exp(-i\mathbf{m}\cdot\mathbf{r}_j) = \sum_{j=1}^{N} q_j \exp\left[-2\pi i\left(\frac{m_1 u_{1j}}{N_1} + \frac{m_2 u_{2j}}{N_2} + \frac{m_3 u_{3j}}{N_3}\right)\right]. \quad (16)$$

For real numbers u_α, let $[u_\alpha]$ denote the integer part of u_α, that is, the unique integer satisfying $[u_\alpha] < u_\alpha < [u_\alpha]+1$. Using linear interpolation, we can approximate the individual exponentials on the right hand side of Eq. 16 by

$$\exp\left(-2\pi i\frac{m_\alpha u_\alpha}{N_\alpha}\right) \approx (1-(u_\alpha-[u_\alpha]))\exp\left(-2\pi i\frac{m_\alpha [u_\alpha]}{N_\alpha}\right) + (u_\alpha-[u_\alpha])\exp\left(-2\pi i\frac{m_\alpha([u_\alpha]+1)}{N_\alpha}\right). \quad (17)$$

Let $W(u)$ denote the linear hat function given by $W(u) = 1-|u|$ for $|u|<1$, $W(u)=0$ for $|u|>1$. Then we can rewrite Eq. 17 as

$$\exp\left(-2\pi i\frac{m_\alpha u_\alpha}{N_\alpha}\right) \approx \sum_{k=-\infty}^{\infty} W(u_\alpha - k_\alpha)\exp\left(-2\pi i\frac{m_\alpha k_\alpha}{N_\alpha}\right), \quad (18)$$

where k_α is integer. The complex exponentials can be written as the fast Fourier transform of charge densities defined at the lattice points as

$$\begin{aligned}
&\sum_{j=1}^{N} q_j \exp(-i\mathbf{m}\cdot\mathbf{r}_j) \\
&= \sum_{j=1}^{N} q_j \sum_{k_1=-\infty}^{\infty}\sum_{k_2=-\infty}^{\infty}\sum_{k_3=-\infty}^{\infty} W(u_{1j}-k_1)W(u_{2j}-k_2)W(u_{3j}-k_3) \\
&\exp\left(-2\pi i\frac{m_1 k_1}{N_1}\right)\exp\left(-2\pi i\frac{m_2 k_2}{N_2}\right)\exp\left(-2\pi i\frac{m_3 k_3}{N_3}\right) \\
&= \sum_{k_1=0}^{N_1-1}\sum_{k_2=0}^{N_2-1}\sum_{k_3=0}^{N_3-1} Q(k_1,k_2,k_3)\exp\left[-2\pi i\left(\frac{m_1 k_1}{N_1}+\frac{m_2 k_2}{N_2}+\frac{m_3 k_3}{N_3}\right)\right] \\
&= F(Q)(m_1,m_2,m_3). \quad (19)
\end{aligned}$$

The charge density $Q(l_1,l_2,l_3)$ at lattice point $\mathbf{l}$ is

$$Q(l_1,l_2,l_3) = \sum_{j=1}^{N} q_j W(u_{1j}-l_1)W(u_{2j}-l_2)W(u_{3j}-l_3). \quad (20)$$

The electrostatic potentials at reciprocal space $\hat{\psi}^L$ can be calculated by the three dimensional fast Fourier transform

$$\begin{aligned}
\hat{\psi}^L(\mathbf{m}) =& 4\pi k_B T l_B \frac{\exp(-\mathbf{m}^2/4\alpha^2)}{V\mathbf{m}^2}\sum_{j=1}^{N} q_j \exp(-i\mathbf{m}\cdot\mathbf{r}_j) \\
=& C(\mathbf{m})F(Q)(m_1,m_2,m_3), \quad (21)
\end{aligned}$$

with the expression of $C(\mathbf{m}) = 4\pi k_B T l_B \exp(-\mathbf{m}^2/4\alpha^2)/V\mathbf{m}^2$.

APPENDIX B

The short-range electrostatic potential is divergent at zero distance, therefore, the collective short-range electrostatic potential at lattice points can not be calculated directly by

$$\psi^S(l_1,l_2,l_3) = k_B T l_B \sum_j \frac{q_j \mathrm{erfc}(\alpha|\mathbf{r}_{l_1,l_2,l_3}-\mathbf{r}_j|)}{|\mathbf{r}_{l_1,l_2,l_3}-\mathbf{r}_j|}. \quad (22)$$

For mean field interactions, it should be approximated to remove the divergency. According to the distance dependence, we approximate the short-range electrostatic potential to be a linearly decaying form as

$$\begin{aligned}
&\psi^S(l_1,l_2,l_3) \\
&= k_B T l_B \frac{\mathrm{erfc}(\alpha\sigma)}{\sigma}\sum_j q_j\left(1 - f\sqrt{(u_{1j}-l_1)^2+(u_{2j}-l_2)^2+(u_{3j}-l_3)^2}\right) \\
&\text{for } |u_{\alpha j}-l_\alpha| \le 1, \quad (23)
\end{aligned}$$

where σ is the diameter of charged particles, $k_BTl_B\mathrm{erfc}(\alpha\sigma)/\sigma$ is adhesion energy, and f is a parameter, chosen to keep

$$\frac{\mathrm{erfc}(\alpha\sigma)}{\sigma}(1-f\sqrt{3}) = \frac{\mathrm{erfc}(\alpha\sqrt{3}H)}{\sqrt{3}H} \tag{24}$$

at $|u_1 - l_1| = |u_2 - l_2| = |u_3 - l_3| = 1$, where $H = |\mathbf{L}|/N$ is the side length of subcell. For most parameter fields used in this work, the parameter f is in a range of $0.3 \sim 0.35$. To comply with the formulism of PF, we need to further approximate Eq. 23 to be

$$\begin{aligned}
&\psi^S(l_1,l_2,l_3)\\
&= k_BTl_B\frac{\mathrm{erfc}(\alpha\sigma)}{\sigma}\sum_j q_jZ_{AP}W(u_{1j}-l_1)W(u_{2j}-l_2)W(u_{3j}-l_3)\\
&= k_BTl_B\frac{\mathrm{erfc}(\alpha\sigma)}{\sigma}Z_{AP}Q(l_1,l_2,l_3)\,,
\end{aligned} \tag{25}$$

where Z_{AP} is a parameter to keep equivalence of Eq. 25 with Eq. 23 in mean field framework. By integration of the space of a subcell, we can obtain the value of Z_{AP} by

$$\begin{aligned}
&\int_0^1\int_0^1\int_0^1 Z_{AP}W(x)W(y)W(z)dxdydz\\
&= \int_0^1\int_0^1\int_0^1 (1-f\sqrt{x^2+y^2+z^2})dxdydz\,.
\end{aligned} \tag{26}$$

The integration results in $Z_{AP} = 8(1-0.96f)$. Thereby, Z_{AP} is in a range of $5.3 \sim 5.7$, which is very close to the coordination number of 6 in three-dimension.

References

1 P. L. Freddolino, A. S. Arkhipov, S. B. Larson, A. McPherson and K. Schulten, *Structure*, 2006, **14**, 437–449.

2 B. R. Brooks, C. L. Brooks, A. D. Mackerell, L. Nilsson, R. J. Petrella, B. Roux, Y. Won, G. Archontis, C. Bartels, S. Boresch, A. Caflisch, L. Caves, Q. Cui, A. R. Dinner, M. Feig, S. Fischer, J. Gao, M. Hodoscek, W. Im, K. Kuczera, T. Lazaridis, J. Ma, V. Ovchinnikov, E. Paci, R. W. Pastor, C. B. Post, J. Z. Pu, M. Schaefer, B. Tidor, R. M. Venable, H. L. Woodcock, X. Wu, W. Yang, D. M. York and M. Karplus, *J. Comput. Chem.*, 2009, **30**, 1545–1614.

3 R. Salomon-Ferrer, D. A. Case and R. C. Walker, *Wiley Interdiscip. Rev. Comput. Mol. Sci.*, 2013, **3**, 198–210.

4 D. Reith, M. Pütz and F. Müller-Plathe, *J. Comput. Chem.*, 2003, **24**, 1624–1636.

5 G. Milano and F. Müller-Plathe, *J. Phys. Chem. B*, 2005, **109**, 18609–18619.

6 C. Peter and K. Kremer, *Soft Matter*, 2009, **5**, 4357–4366.

7 H. A. Karimi-Varzaneh, N. F. A. van der Vegt, F. Müller-Plathe and P. Carbone, *ChemPhysChem*, 2012, **13**, 3428–3439.

8 Z. Wu, Q. Cui and A. Yethiraj, *J. Phys. Chem. B*, 2013, **117**, 12145–12156.

9 T. Chen, H.-J. Qian, Y.-L. Zhu and Z.-Y. Lu, *Macromolecules*, 2015, **48**, 2751–2760.

10 L. Monticelli, S. K. Kandasamy, X. Periole, R. G. Larson, D. P. Tieleman and S.-J. Marrink, *J. Chem. Theory Comput.*, 2008, **4**, 819–834.

11 H. A. Karimi-Varzaneh, H.-J. Qian, X.-Y. Chen, P. Carbone and F. Müller-Plathe, *J. Comput. Chem.*, 2011, **32**, 1475–1487.

12 A. P. Lyubartsev and A. Laaksonen, *Phys. Rev. E*, 1995, **52**, 3730–3737.

13 R. Potestio, S. Fritsch, P. Español, R. Delgado-Buscalioni, K. Kremer, R. Everaers and D. Donadio, *Phys. Rev. Lett.*, 2013, **110**, 108301.

14 G. J. A. Sevink, M. Charlaganov and J. G. E. M. Fraaije, *Soft Matter*, 2013, **9**, 2816–2831.

15 K. C. Daoulas, M. Müller, J. J. de Pablo, P. F. Nealey and G. D. Smith, *Soft Matter*, 2006, **2**, 573–583.

16 M. Müller and K. C. Daoulas, *Phys. Rev. Lett.*, 2011, **107**, 227801.

17 F. A. Detcheverry, H. Kang, K. C. Daoulas, M. Müller, P. F. Nealey and J. J. de Pablo, *Macromolecules*, 2008, **41**, 4989–5001.

18 P. K. Jha, J. W. Zwanikken, F. A. Detcheverry, J. J. de Pablo and M. Olvera de la Cruz, *Soft Matter*, 2011, **7**, 5965–5975.

19 M. P. Stoykovich, M. Müller, S. O. Kim, H. H. Solak, E. W. Edwards, J. J. de Pablo and P. F. Nealey, *Science*, 2005, **308**, 1442.

20 K. M. Langner and G. J. A. Sevink, *Soft Matter*, 2012, **8**, 5102–5118.

21 P. G. Khalatur, in *Polymer Science: A Comprehensive Reference*, ed. K. M. Möller, Elsevier, Amsterdam, 2012, pp. 417–460.

22 M. Giuseppe, K. Toshihiro and A. De Nicola, *Phys. Biol.*, 2013, **10**, 045007.

23 G. Milano and T. Kawakatsu, *J. Chem. Phys.*, 2009, **130**, 214106.

24 Y. Zhao, A. De Nicola, T. Kawakatsu and G. Milano, *J. Comput. Chem.*, 2012, **33**, 868–880.

25 A. De Nicola, Y. Zhao, T. Kawakatsu, D. Roccatano and G. Milano, *J. Chem. Theory Comput.*, 2011, **7**, 2947–2962.

26 A. De Nicola, Y. Zhao, T. Kawakatsu, D. Roccatano and G. Milano, *Theor. Chem. Acc.*, 2012, **131**, 1–16.

27 A. De Nicola, T. Kawakatsu and G. Milano, *Macromol. Chem. Phys.*, 2013, **214**, 1940–1950.

28 A. De Nicola, S. Hezaveh, Y. Zhao, T. Kawakatsu, D. Roccatano and G. Milano, *Phys. Chem. Chem. Phys.*, 2014, **16**, 5093–5105.

29 A. De Nicola, T. Kawakatsu and G. Milano, *J. Chem. Theory Comput.*, 2014, **10**, 5651–5667.

30 G. Decher and J. Schlenoff, *Multilayer Thin Films*, 2nd edn, Wiley-VCH, Weinheim, 2012.

31 Y. Li, X. Wang and J. Sun, *Chem. Soc. Rev.*, 2012, **41**, 5998–6009.

32 P. P. Ewald, *Annalen der Physik*, 1921, **369**, 253–287.

33 L. Greengard and V. Rokhlin, *J. Comput. Phys.*, 1997, **135**, 280–292.

34 A. C. Maggs and V. Rossetto, *Phys. Rev. Lett.*, 2002, **88**, 196402.

35 I. Nakamura and Z.-G. Wang, *Soft Matter*, 2013, **9**, 5686–

5690.
36 J. V. L. Beckers, C. P. Lowe and S. W. D. Leeuw, *Mol. Simul.*, 1998, **20**, 369–383.
37 T. Darden, D. York and L. Pedersen, *J. Chem. Phys.*, 1993, **98**, 10089–10092.
38 U. Essmann, L. Perera, M. L. Berkowitz, T. Darden, H. Lee and L. G. Pedersen, *J. Chem. Phys.*, 1995, **103**, 8577–8593.
39 Y.-L. Wang, A. Laaksonen and Z.-Y. Lu, *Phys. Chem. Chem. Phys.*, 2013, **15**, 13559–13569.
40 Y.-L. Wang, F. Hedman, M. Porcu, F. Mocci and A. Laaksonen, *Applied Mathematics*, 2014, **5**, 520–541.
41 Y.-L. Zhu, H. Liu, Z.-W. Li, H.-J. Qian, G. Milano and Z.-Y. Lu, *J. Comput. Chem.*, 2013, **34**, 2197–2211.
42 A.-C. Shi and J. Noolandi, *Macromol. Theory Simul.*, 1999, **8**, 214–229.
43 Q. Wang, *Soft Matter*, 2009, **5**, 413–424.
44 S. Pronk, S. Páll, R. Schulz, P. Larsson, P. Bjelkmar, R. Apostolov, M. R. Shirts, J. C. Smith, P. M. Kasson, D. van der Spoel, B. Hess and E. Lindahl, *Bioinformatics*, 2013, **29**, 845–854.
45 L. J. Liu, J. Z. Chen, W. D. Chen, L. Y. Li and L. J. An, *Sci. China Chem.*, 2014, **57**, 1048–1052.
46 A.-V. G. Ruzette, P. P. Soo, D. R. Sadoway and A. M. Mayes, *J. Electrochem. Soc.*, 2001, **148**, A537–A543.
47 H. Lee, A. H. de Vries, S.-J. Marrink and R. W. Pastor, *J. Phys. Chem. B*, 2009, **113**, 13186–13194.
48 C. Chen, P. Depa, J. K. Maranas and V. G. Sakai, *J. Chem. Phys.*, 2008, **128**, 124906.
49 J. Wang and T. Hou, *J. Comput. Chem.*, 2011, **32**, 3505–3519.
50 D. Mu, X.-R. Huang, Z.-Y. Lu and C.-C. Sun, *Chem. Phys.*, 2008, **348**, 122–129.
51 I. Nakamura and Z.-G. Wang, *ACS Macro Lett.*, 2014, 708–711.
52 C. E. Sing, J. W. Zwanikken and M. O. de la Cruz, *Nat. Mater.*, 2014, **13**, 694–698.
53 H. Lee, R. M. Venable, A. D. M. Jr and R. W. Pastor, *Biophys. J.*, 2008, **95**, 1590–1599.
54 W.-S. Young, J. N. L. Albert, A. B. Schantz and T. H. Epps, *Macromolecules*, 2011, **44**, 8116–8123.
55 J. Huang, Z.-Z. Tong, B. Zhou, J.-T. Xu and Z.-Q. Fan, *Polymer*, 2014, **55**, 1070–1077.